Oceanic Anoxic Event 2 triggered by Kerguelen Plateau volcanism

Chloe Walker-Trivett (✉ cw725@exeter.ac.uk)

The University of Exeter   https://orcid.org/0000-0002-1630-2076

Sev Kender

University of Exeter   https://orcid.org/0000-0003-4216-3214

Kara Bogus

University of Exeter

Kate Littler

University of Exeter

Trine Edvardsen

University of Exeter

Melanie Leng

British Geological Survey

Jack Lacey

British Geological Survey   https://orcid.org/0000-0002-6329-2149

Article

Keywords:

Abstract

Large Igneous Province (LIP) volcanism is thought to have been the main cause of global warming, ocean anoxia and carbon cycle perturbations associated with Cretaceous Oceanic Anoxic Event 2 (OAE2, ~94 Ma). However, there is still no consensus on the timing and role volcanism played in triggering carbon cycle changes, or the source of the volcanism that has been previously ascribed to either the Caribbean LIP or High Arctic LIP. Here, we refine the stratigraphic position of OAE2 and the Mid-Cenomanian Event (MCE, ~96.5 Ma) at two sites in the Mentelle Basin (offshore southwestern Australia), and use sedimentary mercury (Hg) abundance to determine the timing of volcanism. Contrary to many Northern Hemisphere records, we report elevated levels of Hg and Hg/total organic carbon (TOC), suggesting OAE2 was initiated by a volcanic source proximal to the Mentelle Basin, such as the Kerguelen LIP. Distinct Hg/TOC pulses preceding the onset of OAE2, and in conjunction with its main phase, suggest volcanic emissions played a central role in triggering and controlling climatic and carbon cycle changes within OAE2. By contrast, we find little evidence to suggest a Southern Hemisphere volcanic episode initiated the MCE. Benthic foraminiferal assemblages and bulk sediment isotopes indicate volcanism caused elevated productivity and probable upwelling in the Southern Hemisphere Mentelle Basin for the duration of OAE2, similar to Northern Hemisphere records.

Main

Oceanic Anoxic Event 2 (OAE2) occurred at the Cenomanian/Turonian boundary (~ 94 Ma) in the mid-Cretaceous during super-hot-house conditions, characterised by high atmospheric CO_2 and exceptionally high sea levels[1]. It was one of several periods of widespread ocean anoxia during the Mesozoic[2], and was coupled with deposition of organic-rich shales, marine extinctions[2,3] and terrestrial vegetation changes[4]. It is often expressed in the sedimentary record as a short-lived negative $\delta^{13}C$ carbon isotope excursion (CIE)[5] followed by a broad positive CIE in bulk organic matter (~ 5‰) and carbonate (2−3‰), although organic carbon isotopes do not always mirror carbonate trends[6]. The Mid-Cenomanian Event (MCE) is a smaller-scale, short-term anoxic event that occurred ~ 96.5 Ma, with a positive $\delta^{13}C$ excursion ~ 1‰[7,8], and a shift in foraminiferal, radiolarian, and calcareous nannofossil assemblages[9,10]. Initiation of OAE2 warming is thought to have enhanced nutrient cycling and stimulated high productivity, explaining the deposition of organic-rich material, the broad positive CIE, and the expansion of oxygen minimum zones (OMZs) due to enhanced decomposition within the water column[11]. This mechanism may also apply to the MCE but the event has hitherto been less comprehensively studied.

One mechanism proposed to have initiated OAE climate change is large-scale volcanism. During the Cretaceous there were several active Large Igneous Provinces (LIPs), including the Caribbean (CLIP; ~95−83 Ma and ~ 81−71 Ma), High Arctic (HALIP; ~130−90 Ma), and Kerguelen (~ 122−90 Ma) (Fig. 1). Each of these LIPs have major eruptive phase timings compatible with OAE2 and MCE initiation, although precise correlation between volcanism and these perturbations is under debate[12−14]. The evidence traditionally used to infer volcanism during OAE2 is sedimentary shifts in osmium (Os) isotopes, with

many sections worldwide found to exhibit a characteristic negative Os_i ($^{187}Os/^{188}Os$) shift from radiogenic (continental weathering) to unradiogenic (hydrothermal alteration and/or weathering of juvenile crust) values, and an increase in sedimentary Os concentrations[6,11, 15–17]. Over OAE2, negative Os_i shifts are variable between sites, and sometimes occurred in multiple pulses immediately prior to and within the event in the Western Interior Seaway (WIS), (proto-)North Atlantic Ocean, Tethys Ocean, European Epicontinental Sea, (proto-)South Atlantic Ocean, and the Pacific Ocean[6,11,16,18]. Identifying the precise OAE2 onset is critical to the debate but remains challenging in many records, particularly those without both carbonate and organic carbon isotope stratigraphy. High concentrations of Os in the WIS[18] and Canadian High Arctic[19] occur shortly after the initiation of a major phase of HALIP volcanism dated to ~ 94 Ma[13], potentially linking it with OAE2[18]. Other studies suggest that the CLIP was the trigger for OAE2[20,21], based on higher Os concentrations and large initial Os_i excursions in the southern WIS adjacent to the Caribbean, compared to sites in the Western Pacific and the central WIS[6].

Sedimentary Hg is potentially a more direct proxy than Os isotopes for LIPs[21,25, 28–30] as it is produced in large quantities by volcanism (accounting for 20–40% of modern natural Hg atmospheric emissions[31]), and exhibits a short residence time in the atmosphere (< 1 year[32]) and oceans (decades to centuries[33]). The short timeframe of atmospheric mixing may allow for globally preserved heterogenous signals from massive subaerial volcanic Hg emissions, whilst submarine volcanism sourced from hydrothermal vents or expelled fluids from reactions between mafic rocks and seawater may cause more regional marine Hg signals[21,28]. After atmospheric emission, precipitation and dust-fall removes Hg, which is either deposited directly into the ocean, or first on land where it is cycled through organic matter and clay and later released into oceans via riverine transport[21]. Following marine emission, Hg is likely to remain within ocean water, either staying proximal to the source or transported distally with ocean currents. Modelling suggests the majority of Hg is sequestered in sediments within < 1 kyr[34]. The relatively modest OAE2 increases in Hg and Hg relative to total organic carbon (Hg/TOC) – the material on which Hg is primarily adsorbed[29] – in the WIS and (proto-)North Atlantic is surprising if OAE2 was triggered by the nearby CLIP[21]. Furthermore, the magnitude of Hg/TOC values from OAE2 sections in the Tethys Ocean indicate no evidence for significant volcanic-related excess Hg[25]. MCE initiation is understudied, and no consensus on LIP involvement has yet been reached[21,35,36].

Here, we measure Hg and Hg/TOC at two high palaeolatitude (~ 60°S) sites in the Mentelle Basin[37] – located relatively close to the Kerguelen LIP (Fig. 1) – over OAE2 and the MCE in order to constrain the possible source and timing of large volcanic episodes. International Ocean Discovery Program (IODP) Sites U1516 and U1513 contain expanded Cenomanian sections in a relatively deep water bathyal setting[37], ideal for Hg analysis. To compare volcanic pulses with regional and global environmental changes, we stratigraphically constrain OAE2 and the MCE within an existing biostratigraphic framework using $\delta^{13}C$ on bulk rock carbonate, TOC, and single species of benthic foraminifera, and then constrain environmental changes with $\delta^{13}C$ and $\delta^{18}O$, benthic foraminiferal assemblages, and other published

productivity proxies. We find higher Hg and Hg/TOC values associated with OAE2 initiation than in Caribbean records, indicating volcanic activity near the Mentelle Basin, such as the Kerguelen LIP. Based on Hg/TOC pulse timings, we suggest volcanic emissions played a significant role in triggering changes in the climate and carbon cycle, as well as regulating the phases of OAE2. In contrast, there is little evidence that the MCE began with a volcanic event near the Mentelle Basin. We infer high productivity and possible upwelling throughout OAE2, based on benthic foraminiferal assemblages and bulk sediment isotopes, similar to Northern Hemisphere records[21,35,36].

Mentelle Basin OAEs

We correlate Sites U1513 and U1516 (Fig. 2; Supplementary Fig. 1) with new tie points (A−I) using a combination of $\delta^{13}C_{(carbonate)}$, $\delta^{13}C_{(organic)}$, Natural Gamma Radiation (NGR), TOC, XRF-Ca counts, and published nannofossil and foraminifera datums ranging from Albian to Turonian (Methods). The sites are ~ 40 km apart and record similar environmental and palaeoceanographic histories. Both are characterised by a broad transition from alternations of (nannofossil-rich) claystones and chalks with relatively higher TOC in the Albian and Cenomanian, punctuated by rare and thin organic-rich shales, to chalk and nannofossil-rich clay in the Turonian with lower TOC. Both the MCE and OAE2 are clearly defined by positive excursions in $\delta^{13}C$ and NGR (Fig. 3).

As $^{13}C_{(carbonate)}$ and $^{13}C_{(organic)}$ records do not exhibit the clear characteristic long-term positive CIE often defining OAE2, due in part to a low carbonate horizon and likely changing sources of bulk material, we constructed a composite benthic foraminiferal isotope record for Site U1516 (Fig. 3) using individual species and correcting for species-specific offsets (Methods, Supplementary Data 1, Supplementary Fig. 2). $^{13}C_{(benthic)}$ and $^{18}O_{(benthic)}$ composite curves reflect bottom water values, and broadly support $^{13}C_{(carbonate)}$ as most likely dominated by a surface water signal from mixed nannofossil and planktonic foraminifera. A notable and clear initial negative $^{13}C_{(carbonate)}$ 'pulse' of ~ 0.75‰ at U1513 and U1516 (tie point F in Fig. 2, phase A in Fig. 3) is also present in OAE2 records from Tibet and Japan, and is taken to mark the onset of OAE2[5,41]. This is followed by the OAE2 'build-up' phase B, a positive CIE which is only partly present due to very low carbonate (from tie point G). The peak CIE is not recorded at either site due low carbonate, but above this interval (from tie point H) elevated $^{13}C_{(benthic)}$ clearly indicates the OAE2 'plateau' phase C, in contrast to the rapid decline in $^{13}C_{(carbonate)}$. This is supported by nannofossil biostratigraphy[38], as *E. octopetalus* first occurrence (FO) and *Q. gartnerii* FO are in OAE2 phase C at sites on Kerguelen Plateau and Eastbourne[25], UK (Fig. 3). The offset of $^{13}C_{(carbonate)}$ from $\delta^{13}C_{(benthic)}$ may be due to a change in the composition of the bulk carbonate (e.g., nannofossil assemblage shift) or change in surface water mass. A gradual decline of ^{13}C in both bulk and benthic foraminiferal records shows the start of the 'recovery' phase D.

Sedimentary Hg reflects Kerguelan LIP activity

Both absolute Hg concentrations and Hg/TOC from Sites U1513 and U1516 (Fig. 2) show significant pulsed enrichments (Hg > 150 ppb and Hg/TOC > 200 ppb/wt%) broadly mirroring one another in association with the lead-up to and early OAE2, compared to low baseline values in the Albian and lower Cenomanian (Hg ~ 50 ppb and Hg/TOC < 100 ppb/wt%). An episode of elevated but minor single-point spikes occurs in the lead-up to OAE2 (above tie point E), a significant long-lived Hg/TOC spike is present during the negative ^{13}C 'pulse' (tie point F in Fig. 2, 'i' in Fig. 4), and a second major spike occurs just after the onset of the low carbonate horizon (tie point G in Fig. 2, 'ii' in Fig. 4). We conclude these Hg pulses originated predominantly from volcanic activity rather than transported terrigenous material common in marginal settings[34], or from buried redox fronts[25]; as our sites were in deep water distal to the shoreline[37], there is no correlation between Hg and proxies for terrigenous input[42] (εNd and K/Al; Supplementary Fig. 4), and no turbiditic sedimentary features are reported[37]. Furthermore, although recent work has suggested euxinic conditions can result in the overprinting of sedimentary Hg[25], we report a lack of isorenieratene indicating no photic zone euxinia (Supplementary Fig. 5), and benthic foraminiferal assemblages indicative of oxic environments below the OAE2 low carbonate interval (Fig. 5). Hg measurements across possible anoxic episodes such as TOC spikes (lower in the low carbonate interval) may therefore be taken as minimum values.

Southern WIS and Demerara Rise records over OAE2 show relatively low Hg (mostly < 100 ppb) and Hg/TOC elevations (mostly < 50 ppb/wt%) (Fig. 4)[21,25], suggesting a Southern Hemisphere volcanic source for the Mentelle Basin spikes. The high Hg/TOC values are more similar to records spanning the end-Triassic Central Atlantic Magmatic Province and OAE1d[30,44] (> 200 ppb/wt%) which, when coupled with their stratigraphic appearance at the beginning of OAE2, point to a nearby volcanic source capable of triggering global climate change such as the Kerguelen LIP (Fig. 1). This LIP was volcanically active for > 32 myr and although precise dating is relatively limited, recent ^{40}Ar/^{39}Ar dating shows an active eruptive phase of the Central Kerguelen Plateau at 92.8 ± 1.5 Ma[14]. The Hg/TOC record from nearby Kerguelen Plateau Ocean Drilling Program Site 1138 shows higher values than North Atlantic sites, but is missing the critical OAE2 onset interval due to a hiatus[24,25] where we might expect elevated Hg (Fig. 4). Hiatuses are perhaps unsurprising as uplift likely occurred during eruptive phases, and the Kerguelen Plateau was largely subaerial with pyroclastic deposits evidencing explosive subaerial volcanism in the Late Cretaceous[45].

Estimating the submarine versus subaerial proportion of Kerguelen Plateau flood basalts is difficult, although extensive evidence exists for both[45]. Volcanic activity associated with the Hg and Hg/TOC spikes across OAE in the Mentelle Basin may have been largely marine-based due to the stronger local signal, although the modest increases in Hg/TOC in Atlantic records[21] may indicate a partial atmospheric signature. The tholeiitic basalts are thought to have contained significant quantities of sulfur[45], and by implication Hg[31] and, similar to CLIP, have Pb isotope values[14,45] similar to those measured across OAE2 in central Italy[46]. The high latitude position of Kerguelen would have allowed injection of gasses and ash directly into the stratosphere, promoting the global influence of atmospheric volatiles[45]. Palaeo-currents

likely influenced the spread of Hg within the ocean basin, and thus the concentration of volcanically-derived Hg in sediments proximal to the source. The palaeogeography of the Cenomanian/Turonian prevented deep water flow between the proto-Indian Ocean and the proto-South Atlantic, the Pacific and the northern Tethys, and restricted intermediate depth currents connecting these regions (Fig. 1)[47,48]. Based on modelled reconstructions of Cretaceous ocean currents, intermediate water may have had a net eastward flow from the Kerguelen Plateau providing a plausible pathway for marine Hg to enter the Mentelle Basin[48].

Evolution of Cenomanian volcanism

There are slightly elevated levels of Hg and Hg/TOC in the lower part of the MCE, relative to background values, at both Mentelle Basin sites (Fig. 2). Although these changes are small (~ 50–100 ppb/wt%), they are similar to those found in other sites that capture the MCE in the proto-North Atlantic and WIS[21]. In the Mentelle Basin Hg and Hg/TOC values are slightly elevated at the onset of the MCE CIE, before dropping to background levels mid-way through. However, this is in contrast to records from the Maverick Basin (southern WIS) and Demerara Rise (proto-North Atlantic), where elevated Hg/TOC values occur mid-way through the CIE[21]. Despite an absence of low Os_i values, indicating volcanism may not have been the primary driver[8, 12–14], our Hg records suggest volcanism may have had a role in triggering the MCE, although the source was likely distal to the Mentelle Basin.

Os records over OAE2 are somewhat different from Hg/TOC records (Fig. 4), in part due to their geographic separation and sedimentary weathering inputs, and in part due to the much longer ocean residence time for Os (~ 10 kyr)[49]. It is also challenging to correlate precisely between sites because biostratigraphy has some uncertainty on short timescales, and the characteristic CIE used to define the OAE2 onset is usually measured on bulk sediment. Indeed, $^{13}C_{(organic)}$ and $^{13}C_{(carbonate)}$ records commonly diverge from one another with the former exhibiting a delayed or absent positive CIE (e.g., Mentelle Basin, Tibet, Vocantian Basin; Fig. 4), whilst important sites from the WIS are based solely on $^{13}C_{(organic)}$. A recent study used $^{13}C_{(organic)}$ to correlate an early Os_i shift in the WIS site Iona-1 as evidence for CLIP activity[6], but we note alternative correlations exist[18]. Furthermore, it is likely that successive Kerguelen LIP eruptive phases released varying relative proportions of Os and Hg, as considerable geochemical variability is detected between different eruptive phases due to changes in relative melt incorporation of plume, continental and oceanic crust[45]. The numerous Hg/TOC pulses between tie points E and F (Fig. 2) document early volcanic activity, and although this is not recorded in Os isotopes from U1516[50] (possibly due to low resolution), precursor negative Os_i excursions do occur in Tibet, the WIS, and Japan[6,16,51] (Fig. 4). This precursor OAE2 volcanism was likely relatively minor as it occurred before major climate changes associated with OAE2, whilst Hg 'spike i' was relatively major as it is more stratigraphically extensive (multiple data points at both sites, Fig. 2), occurs at the beginning of the Os_i excursion in U1516 (Fig. 4), and is associated with the initial negative ^{13}C 'pulse' of OAE2 phase A (Figs. 2–4). A similar sharp negative shift has also been documented in England[52], the southeast North

Atlantic[53], the western Pacific[54] and the WIS[55], and has been suggested as linked to LIP-related carbon release[5].

Volcanism-induced palaeoenvironmental change over OAE2

Kerguelen LIP carbon release[45] likely caused ocean warming, which in the Cretaceous may have disrupted the thermocline, triggering upwelling nutrient-rich waters to sustain enhanced productivity[56]. Between 478–474 m in U1516 (Fig. 6), the dominance of opportunistic planktonic foraminifera *Microhedbergella* has been interpreted as signifying enhanced nutrient runoff and likely upwelling[38], and our benthic foraminiferal assemblage data supports changing organic carbon flux with varying infaunal/high productivity species ranging from 5–40%. To test for upwelling, we calculated the difference between measured $^{13}C_{(organic)}$ and $^{13}C_{(carbonate)}$ values in the same sample ($\Delta^{13}C$) as a proxy for relative changes in surface ocean CO_2[57]. Our data shows a gradual and sustained divergence (increased $\Delta^{13}C$) in the lead up to and early OAE2 phases A and B (Fig. 6), supporting enhanced upwelling bringing CO_2-rich water to the surface, and/or increasing atmospheric CO_2[58], possibly linked to volcanism.

The second significant Hg and Hg/TOC 'spike II' (Fig. 4, 6) occurs near the base of the low carbonate interval, and likely identifies a significant episode of LIP volcanism due to its association with severe environmental change in the Mentelle Basin (e.g., ocean acidification[50] and an enhanced hydrological cycle[59]), and a pulse in Os with low Os_i values in U1516 likely global in nature (Fig. 4). Enhanced productivity (TOC spikes, biogenic silica[50], radiolarians)[38] (Fig. 6) occurred with enhanced upwelling (further decreasing $^{13}C_{(organic)}$) (Fig. 2). Above the low carbonate interval (OAE phase C), benthic foraminiferal assemblages contain a greater proportion of infaunal/high productivity species, increasing % $CaCO_3$, and high productivity *Microhedbergella* and "*Globigerinellioides*"[38], despite the presence of organic poor sediments. Due to low TOC, Hg data are absent, except one point in U1516 which suggests possible further episodes of volcanism through phases B / C (Fig. 6); this is supported by Os and Os_i pulses that occur above the low carbonate interval, suggested as from Kerguelen volcanism[50].

Our work highlights the utility of using multiple volcanic proxies in diagnosing causal mechanisms for past global warming events, and the critical importance of measuring species-specific isotopes in refining global OAE correlations. Future study of Kerguelen Plateau eruptive phases, Hg isotopes and earth system modelling will provide insights into LIP emissions and climate interactions, and identification of past tipping points within the climate system.

Methods

Organic carbon isotope analysis

Sediment samples for isotope analysis on carbonate (calcite) were processed by disaggregating around 1 g of sample in a 500 ml glass beaker containing 5% sodium hypochlorite (NaClO) solution for 24 hours to oxidise any reactive organic matter (OM). This solution was then diluted to 500 ml and rinsed three times with deionised water to remove any remaining NaClO or oxidised OM. After carefully tipping off the majority of deionised water from the final rinse (< 50 ml), the samples were dried at 40°C and subsequently powdered and homogenised in an agate pestle and mortar. The same process was used to prepare samples for isotope analysis of the organic fraction, but with 5% HCl instead of NaClO (as used for calcite), to remove carbonate.

Carbon isotopic (δ^{13}C) analysis of samples was carried out at the National Environmental Isotope Facility at the British Geological Survey (UK) using an Elementar vario ISOTOPE cube elemental analyser (EA) coupled to an isoprime precisION isotope ratio mass spectrometer (IRMS) with an onboard centrION continuous flow interface system. The EA inlet converts organic materials in solid sample matrices into pure gases via high-temperature combustion. The post-combustion gas mixture is then separated and focused into individual molecular species for quantitative analysis of nitrogen and carbon content and are then passed online to the IRMS for the determination of their stable isotope composition. Carbon isotope data are reported in delta (δ) notation in per mille (‰) relative to the international reference scale VPDB. Carbon isotope ratios were corrected using a multi-point calibration against organic analytical standards B2162 (spirulina algae, Elemental Microanalysis Ltd.; −18.7‰, in-house value), B2151 (soil, Elemental Microanalysis Ltd.; −28.9‰), and B2213 (spruce powder, Elemental Microanalysis Ltd.; −25.4‰), and a laboratory working standard (BROC3, − 27.6‰). The reference materials BROC3 and B2162 have been calibrated for δ13C using IAEA-CH-6 (− 10.5‰), USGS54 (− 24.4‰), USGS40 (− 26.4‰), and B2174 (urea, Elemental Microanalysis Ltd.; −36.5‰). External precision (1σ) for the within-run standards and sample repeats was < 0.1‰. BROC3 (41.3%C and 4.9%N) was used to calculate the carbon and nitrogen elemental content of samples.

Carbonate isotope analysis

Total Inorganic Carbon (TIC) is assumed to mainly represent $CaCO_3$ (calcite). The $CaCO_3$ proportion of total sediment weight is calculated by $CaCO_3$ (%) = TIC (%) x 8.33. TIC only represents the carbon atoms in the $CaCO_3$ compound and so to calculate the sediment proportion of $CaCO_3$ a factor of 100.09/12.01 = 8.33 must be applied, where the atomic mass of $CaCO_3$ = 100.09 and carbon = 12.01. The samples will also not contain 100% $CaCO_3$ (due to other inclusions, e.g. inert clastic material), therefore, the final sample weight required for analysis must be calculated to contain 10 mg of $CaCO_3$ using: sample weight (mg) = [100%/$CaCO_3$%]*10 mg. This provides a conservative estimate given TIC is measured before OM is removed.

Each carbonate sample is weighed into a glass vial and placed into a reaction vessel containing anhydrous phosphoric acid (H_3PO_4), which is then attached to the glass vacuum line and evacuated. Once a sufficient vacuum pressure had been achieved (< 8×10^{-5} mbar), the vessels are sealed and

transferred to a water bath at 25°C to equilibrate for at least 15 minutes. The vessels are then overturned, and the sample reacted with the phosphoric acid:

$$3CaCO_3[s] + 2H_3PO_{4[aq]} = Ca_3(PO_4)_{2[aq]} + 3CO_{2[g]} + 3H_2O_{[l]}$$
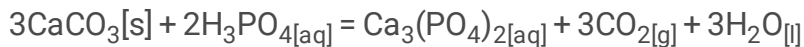
The vessels are then returned to the water bath and left to react for at least 16 hours at a constant 25°C. After allowing enough time for a complete reaction, any remaining water vapour is removed from the liberated CO_2 by passing the gas through a cold trap held at -90°C on the vacuum extraction line. The purified CO_2 is subsequently transferred and frozen into collection vessels submerged in liquid nitrogen and evacuated to $< 2x10^{-5}$ mbar to remove any other gaseous fraction.

The evolved CO_2 was analysed at the National Environmental Isotope Facility at the British Geological Survey (UK) using a VG Optima or Thermo MAT 253 dual inlet mass spectrometer relative to a reference CO_2, where stable isotope measurements are made on CO_2 from both the sample and within-run carbonate standards (internal standards are MCS and CCS). The mass spectrometer measures three mass fractions (44, 45, 46) and these correspond primarily to $44 = {}^{12}C^{16}O_2$, $45 = {}^{13}C^{16}O_2$, and $46 = {}^{12}C^{16}O^{18}O$. $\delta^{13}C$ and $\delta^{18}O$ are calculated from the mass ratios 45/44 and 46/44, respectively, relative to the Vienna Pee Dee Belemnite (VPDB) scale using a single-point anchoring procedure based on calibrated $\delta^{13}C_{MCS-VPDB}$ and $\delta^{18}O_{MCS-VPDB}$ values (via NBS and IAEA international reference materials). A correction is applied to the 45/44 and 46/44 ratios for the minor contribution from ^{17}O on the 45 ($^{12}C^{17}O^{16}O$) and 46 ($^{13}C^{17}O^{16}O$) ion beams[60]. A fractionation factor is also applied to $\delta^{18}O$ as although all carbon is transferred to the evolved CO_2 during reaction with phosphoric acid, only two-thirds of the oxygen is collected. The acid fractionation factor is constant in this case as the oxygen isotope fractionation between the evolved CO_2 and original mineral is temperature-dependent and the reaction is controlled at 25°C using the water bath. The fractionation factor ( ) between CO_2 and calcite during reaction with phosphoric acid at 25°C is 1.01025. Using $\alpha_{CO2-calcite}$ the $\delta^{18}O$ of the original calcite is then calculated using $1.01025 = [1000 + \delta_{CO2}] / [1000 + \delta_{calcite}]^{61}$. The analytical reproducibility calculated from the standard deviation (1σ) of the within-run laboratory standards is typically < 0.1‰ for both $\delta^{18}O$ and $\delta^{13}C$.

Hg analysis

Hg analysis was carried out on 259 bulk sediment samples (145 from Site U1516 and 114 from Site U1513) by an RA 915F Lumex Portable Mercury at the Camborne School of Mines, University of Exeter. Methods were adapted from previous studies[28]. After decarbonisation, to allow consistent normalisation with TOC, approximately 50 mg of sediment powder were measured into a quartz measuring boat and its precise mass determined. Samples were heated in the Pyrolyzer to ~ 700°C to volatilise the Hg within the sample. Following this, gaseous Hg was transported into the Analyzer and abundance was measured, providing the abundance mass of Hg as parts per billion. The Analyser was initially calibrated by measuring 20, 30 and 40 mg of the following international standards: NIST 2682b (37.3 ng/g), NIST

2693 (108.8 ng/g), NIST 2709 (1400 ng/g) and NIST 2711 (6250 ng/g). The resulting calibration curve yields a correlation factor of 0.9996. An additional calibration curve for lower Hg values was then created by repeating NIST 2682b and NIST 2693 five times, which resulted in a correlation factor of 0.9936. An internal standard called PM43, calibrated to these international standards, was used the beginning and end of every run and after every 8 samples during the analytical run to ensure continuity. PM43 has an average Hg concentration of 107 ± 3 ppb and is composed of powdered and homogenised mudrock from a horizon of the Whitby Mudstone Formation, Port Mulgrave, Yorkshire. For this study, the mean value for PM43, recorded from the beginning of each analytical run and the 8-sample interval within-run repeats, was 108.1 ± 3.0 ppb (72 measurements). The average standard deviation of repeated samples was 5.6 ppb (39 repeats). Following Kender *et al.*[21] the minimum possible value for Hg/TOC is represented by: (sample Hg − 1 standard deviation) / (TOC + 1 standard deviation). The highest possible Hg/TOC value is calculated as: (sample Hg + 1 standard deviation) / (TOC − 1 standard deviation). The standard deviation of analytical uncertainty for Hg values is 3 ppb, and for TOC is 0.1%.

For both records, sedimentary Hg shows highly fluctuating values from 0 to 1614 ppb. An organic carbon association for this sedimentary Hg is supported by the relationships between Hg and TOC across all samples from Sites U1513 and U1516, and the very low Hg values in samples with low TOC (Supplementary Fig. 6, A-C). Poor relationships were found ($R^2 < 0.08$) between Hg concentration and XRF counts for Al, S and Fe (Supplementary Fig. 6D-J).

Benthic foraminiferal analyses

A total of 42 samples from Site U1516 were investigated for benthic foraminiferal assemblages (Fig. 5). Two to three samples per core section were collected from Cores U1516D-2R to U1516D-5R, and one to two samples per core section were collected from Cores U1516C-32R to U1516C-35R-1W. All samples of approximately 20−30 cc were disaggregated completely by screen-washing at 63 µm, and oven dried at low temperature following standard procedures. All specimens were picked into cardboard reference slides from the > 63 µm fraction and identified to species level where possible. Preservation is moderate to poor and in some cases identification could only be made to the generic level. The suprageneric classification follows Loeblich and Tappan (1988)[62] while the taxonomic concept mainly follows Belford (1960)[63], Hanzlikova (1969)[64] and Holbourn and Kuhnt (2002)[65]. Benthic foraminiferal ranges are illustrated in Supplementary data 2, and names and references in the taxonomic list. Key species were imaged after carbon coating using a TESCAN VEGA3 GMU SEM at the Penryn Campus, University of Exeter (Supplementary Fig. 7). The figured specimens are stored in Copenhagen, Denmark (contact author T. Edvardsen for details).

Statistical Correspondence Analysis (CA) and Fisher's Alpha (α) diversity was carried out on the entire benthic foraminiferal dataset using the software PAST v. 2.17c[66]. Fisher's Alpha is used because it is theoretically independent of sample size, as it estimates the area beneath a smoothed curve of a parametric species abundance distribution[67]. Diversity averaged 14 species per sample, and most species of cosmopolitan distribution ranging through water depths of outer neritic to upper bathyal

(Supplementary Table 3). Species were grouped according to their palaeoecology (Supplementary Table 3), with some information from $\delta^{13}C$ (Supplementary Fig. 10), which was used to create the 'Infauna/high productivity %' plot in Fig. 6. CA indicates the most significant assemblage shift occurs either side of the low carbonate horizon, with 26 species restricted to below this, 17 species appearing after, and 28 survivor species persisting throughout the record (Fig. 5). Axis 1 of the CA correlates well with the proportion of infaunal / high productivity species (Supplementary Table 3, Supplementary Fig. 8).

Sample processing and foraminiferal stable isotopes

Measurements of $\delta^{13}C$ and $\delta^{18}O$ of the material were carried out on all 42 samples across 10 species of benthic foraminifera, as there was no single species that occurred in all samples at the required abundance. Contingent on the species, between 1 and 10 specimens per species were measured for each sample (approximately 60 – 100 micrograms of carbonate). Measurements were carried out at the British Geological Survey, using an IsoPrime 100 dual inlet mass spectrometer with a MultiCarb preparation device. The samples were loaded into glass vials and sealed with septa, after which the vials were evacuated and reacted with anhydrous phosphoric acid at 90°C. The evolved CO_2 was collected cryogenically for 15 minutes and passed on-line to the mass spectrometer. Isotope values ($\delta^{13}C$, $\delta^{18}O$) are expressed as per mille deviations of the isotopic ratios ($^{13}C/^{12}C$, $^{18}O/^{16}O$) calculated to the Vienna Pee Dee Belemnite (V-PDB) scale using a within-run laboratory standard (KCM) calibrated against NBS-19. The calcite-acid fractionation factor applied to the gas values is 1.00798. Due to the long run time, a drift correction was applied across the run, calculated using standards that bracketed the samples. The Craig correction[60] was also applied to account for ^{17}O contribution. The average analytical reproducibility of the KCM standard is < 0.1‰ for $\delta^{13}C$ and $\delta^{18}O$.

Composite benthic isotope record

To construct a consistent composite isotope record showing changes in ocean chemistry, we calculated species specific isotopic offsets. Between 471.4 and 479.8 m CCSF-M (a period with little fluctuation in isotopic composition) the average ^{13}C and ^{18}O values were calculated for *Cibicides*, *Gavelinellinae*, *Gyroidinoides* and *Osangularia utaturensis* (Supplementary Figs. 2 and 3). Using these averages, the offset between *Cibicides* and each of the other groups was calculated, and this offset was then applied to all data for each species. Where isotope values for multiple species were available for one depth horizon, the average of these was calculated for use in the final composite curve (see Supplementary data 1).

Statistical methods – XRF

Core scanning XRF data[40] are shown in Figs. 2 and 6. To remove noise a locally-weighted scatterplot smoothing (LOWESS) method has been applied using the software PAST[66]. Samples with both % $CaCO_3$ and Ca count (XRF) data were cross plotted. A linear trendline was calculated for each site, and the linear

equation used to create a secondary axis on figures, which translates Ca counts into approximate % $CaCO_3$ (Supplementary Fig. 9).

Site information

IODP Site U1516 is located at a water depth of 2675 m, and U1513 at 2700 m – both lie in the Mentelle Basin, situated along the western margin of Australia (Supplementary Fig. 1). Holes U1516C and U1516D were drilled with a 20 m offset at 34° 20.9272'S, 112° 47.9711'E and 34° 20.9277'S, 112° 47.9573'E, respectively. Holes U1513A and U1513D were also drilled at with a 20 m offset, at 33°47.6084'S, 112°29.1338'E and 33°47.6196'S, 112°29.1339'E, respectively[37].

For this study, two successions of Cenomanian to Turonian chalk and clay-rich sediments were investigated from two spliced intervals of Holes U1516C and U1516D, and U1513A and U1513D. The splices are made using shipboard RGB colour data and Fe counts from core scanning XRF data to correlate overlapping sections of two holes drilled at the same site, providing a continuous interval unaffected by coring disturbances or poor recovery. All sample depths are reported in meters using the depth scale CCSF-M, which stands for Core Composite depth below Sea Floor, where Method "M" denotes that off-splice intervals are mapped to the splice[68].

IODP Sites U1516 and U1513 both transition from calcareous chalk interbedded with chert (< 470 m and < 234 m, respectively), grading down-section into greenish grey calcareous/nannofossil chalk with clay (Fig. 2). Below this are bands of black, light greenish grey, greenish grey, and very dark greenish grey claystone and clayey nannofossil chalk. Below 480 m (U1516), and 263 m (U1513), is a sequence of massive to mottled black and dark greenish grey nannofossil-rich claystone and claystone with nannofossils (Fig. 2).

A detailed sedimentological description of Site U1516, as well as details on drilling operations, logging, physical properties, magnetostratigraphy, and geochemistry are available in the IODP Expedition 369 proceedings report[37].

Stratigraphy and site correlation

The biostratigraphic markers in Fig. 2 comprise a combination of initial IODP Expedition 369 shipboard biostratigraphy[37] and more recent publications[38,39] (Supplementary Tables 1 and 2). Within this framework, we propose a new refined correlation between Sites U1516 and U1513 based on a combination of existing high resolution data (NGR and XRF) and new high resolution data presented in this study ($^{13}C_{(TOC)}$, $^{13}C_{(carbonate)}$ and TOC).

Tie point A is placed between two peaks in NGR data. Due to core gaps and fewer geochemical data to support the correlation, it is more speculative. A slight excursion in the ^{13}C at Site U1516 and biostratigraphic constraints from *E. turriseiffellii* first occurrence (FO) (U1516) and *Ticinella primula* FO (U1513−306.88−304.91m) suggest that this could represent a low resolution record of OAE 1d, which

occurs during the latest Albian ~101 Ma[2] (Fig. 2). Although more isotope data is needed, our interpretation of OAE 1d coinciding with the clear elevation in NRG is consistent with the stratigraphically higher MCE and OAE2 events.

Tie point B is placed at the onset of a significant positive CIE in $^{13}C_{(TOC)}$ (2‰ at U1513 and 1.5‰ at U1516) and $^{13}C_{(carbonate)}$ (1‰ at U1513 and 2‰ at U1516), and a concurrent spike in NGR data. Biostratigraphic markers indicate an age between 98−96 Ma, consistent with the MCE (96.5 Ma)[8]. In other records, the MCE is defined by a positive CIE ~ 1‰[69], and it is to our knowledge the first reported Southern Hemisphere record of the MCE. Tie point C is placed mid-way through the CIE at the second peak in NGR, and tie point D is placed at the end of the CIE. There is no significant increase in % wt. TOC across this interval, which is reflected in the lack of black shale horizons, however this is not uncommon in MCE sediments from other sites[7]. Tie point E is placed below *G. nanum* last occurrence (LO) when NGR falls to low values, and at the termination of a $^{13}C_{(carbonate)}$ negative CIE, after which stable values persist for > 5 m of sediment core.

Tie point F is placed at the occurrence of a short-lived negative shift in $^{13}C_{(carbonate)}$, modest NGR spike and Ca/Al fall. We interpret this as defining the base of OAE2, in agreement with biostratigraphic markers and recent publications[38,39] (Fig. 3). Tie points G and H are placed at the onset and termination of a low carbonate horizon, interpreted to occur within the OAE2 main phase. Specifically, tie point G is placed at the disappearance of carbonate, a spike in TOC content, elevated NGR and a negative excursion in $^{13}C_{(organic)}$. Tie point H is placed at the termination of the low carbonate interval when Ca/Al values increase from 0 and $^{13}C_{(carbonate)}$ data returns. The final tie point I is placed above *Q. gartneri* FO (near the end of OAE2), at maximum Ca/Al and where $^{13}C_{(carbonate)}$ data begins to decline after a long plateau phase.

References

1. Huber, B. T., MacLeod, K. G., Watkins, D. K. & Coffin, M. F. The rise and fall of the Cretaceous Hot Greenhouse climate. *Glob. Planet. Change* **167**, 1−23 (2018).
2. Jenkyns, H. C. Geochemistry of oceanic anoxic events. *Geochemistry, Geophys. Geosystems* **11**, (2010).
3. Leckie, R. M., Bralower, T. J. & Cashman, R. Oceanic anoxic events and plankton evolution: Biotic response to tectonic forcing during the mid-Cretaceous. *Paleoceanography* **17**, 13-1-13−29 (2002).
4. Heimhofer, U. *et al.* Vegetation response to exceptional global warmth during Oceanic Anoxic Event 2. *Nat. Commun.* **9**, (2018).
5. Takashima, R. *et al.* Prevailing oxic environments in the Pacific Ocean during the mid-Cretaceous Oceanic Anoxic Event 2. *Nat. Commun.* **2**, (2011).

6. Li, Y. X. *et al.* Enhanced ocean connectivity and volcanism instigated global onset of Cretaceous Oceanic Anoxic Event 2 (OAE2) ~94.5 million years ago. *Earth Planet. Sci. Lett.* **578**, (2022).

7. Eldrett, J. S. *et al.* An astronomically calibrated stratigraphy of the Cenomanian, Turonian and earliest Coniacian from the Cretaceous Western Interior Seaway, USA: Implications for global chronostratigraphy. *Cretac. Res.* **56**, 316–344 (2015).

8. Nana Yobo, L. *et al.* Enhanced continental weathering activity at the onset of the mid-Cenomanian Event (MCE). *Geochemical Perspect.* **23**, 17–22 (2022).

9. Coccioni, R. & Galeotti, S. The mid-Cenomanian Event: Prelude to OAE 2. *Palaeogeogr. Palaeoclimatol. Palaeoecol.* **190**, 427–440 (2003).

10. Hardas, P., Mutterlose, J., Friedrich, O. & Erbacher, J. The Middle Cenomanian Event in the equatorial Atlantic: The calcareous nannofossil and benthic foraminiferal response. *Mar. Micropaleontol.* **96–97**, 66–74 (2012).

11. Turgeon, S. C. & Creaser, R. A. Cretaceous oceanic anoxic event 2 triggered by a massive magmatic episode. *Nature* **454**, 323–326 (2008).

12. Dürkefälden, A. *et al.* Age and geochemistry of the Beata Ridge: Primary formation during the main phase (~89 Ma) of the Caribbean Large Igneous Province. *Lithos* **328–329**, 69–87 (2019).

13. Kingsbury, C. G., Kamo, S. L., Ernst, R. E., Söderlund, U. & Cousens, B. L. U-Pb geochronology of the plumbing system associated with the Late Cretaceous Strand Fiord Formation, Axel Heiberg Island, Canada: part of the 130-90 Ma High Arctic large igneous province. *J. Geodyn.* **118**, 106–117 (2018).

14. Jiang, Q., Jourdan, F., Olierook, H. K. H., Merle, R. E. & Whittaker, J. M. Longest continuously erupting large igneous province driven by plume-ridge interaction. *Geology* **49**, 206–210 (2021).

15. Dickson, A. J., Cohen, A. S. & Davies, M. The Osmium Isotope Signature of Phanerozoic Large Igneous Provinces. in *Large Igneous Provinces: A Driver of Global Environmental and Biotic Changes* 229–246 (2021). doi:https://doi.org/10.1002/9781119507444.ch10.

16. Du Vivier, A. D. C. *et al.* Marine 187Os/188Os isotope stratigraphy reveals the interaction of volcanism and ocean circulation during Oceanic Anoxic Event 2. *Earth Planet. Sci. Lett.* **389**, 23–33 (2014).

17. Cohen, A. S. & Coe, A. L. The impact of the Central Atlantic Magmatic Province on climate and on the Sr- and Os-isotope evolution of seawater. *Palaeogeogr. Palaeoclimatol. Palaeoecol.* **244**, 374–390 (2007).

18. Sullivan, D. L. *et al.* High resolution osmium data record three distinct pulses of magmatic activity during cretaceous Oceanic Anoxic Event 2 (OAE-2). *Geochim. Cosmochim. Acta* **285**, 257–273 (2020).

19. Schröder-Adams, C. J., Herrle, J. O., Selby, D., Quesnel, A. & Froude, G. Influence of the High Arctic Igneous Province on the Cenomanian/Turonian boundary interval, Sverdrup Basin, High Canadian Arctic. *Earth Planet. Sci. Lett.* **511**, 76–88 (2019).

20. Snow, L. J., Duncan, R. A. & Bralower, T. J. Trace element abundances in the Rock Canyon Anticline, Pueblo, Colorado, marine sedimentary section and their relationship to Caribbean plateau

construction and oxygen anoxic event 2. *Paleoceanography* **20**, 1–14 (2005).

21. Scaife, J. D. *et al.* Sedimentary Mercury Enrichments as a Marker for Submarine Large Igneous Province Volcanism? Evidence From the Mid-Cenomanian Event and Oceanic Anoxic Event 2 (Late Cretaceous). *Geochemistry, Geophys. Geosystems* **18**, 4253–4275 (2017).

22. Scotese. PALEOMAP PaleoAtlas for GPlates and the PaleoData Plotter Program. *PALEOMAP Proj.* (2016).

23. Whittaker, J. M. *et al.* Long-term interaction between mid-ocean ridges and mantle plumes. *Nat. Geosci.* **8**, 479–483 (2015).

24. Dickson, A. J. *et al.* A Southern Hemisphere record of global trace-metal drawdown and orbital modulation of organic-matter burial across the Cenomanian–Turonian boundary (Ocean Drilling Program Site 1138, Kerguelen Plateau). *Sedimentology* **64**, 186–203 (2017).

25. Percival, L. M. E. *et al.* Does large igneous province volcanism always perturb the mercury cycle? Comparing the records of Oceanic Anoxic Event 2 and the end-Cretaceous to other Mesozoic events. *Am. J. Sci.* **318**, 799–860 (2018).

26. MacLeod, K. G., Martin, E. E. & Blair, S. W. Nd isotopic excursion across Cretaceous ocean anoxic event 2 (Cenomanian-Turonian) in the tropical North Atlantic. *Geology* **36**, 811–814 (2008).

27. Ladant, J.-B. *et al.* Paleogeographic controls on the evolution of Late Cretaceous ocean circulation. *Clim. Past* **16**, 973–1006 (2020).

28. Kender, S. *et al.* Paleocene/Eocene carbon feedbacks triggered by volcanic activity. *Nat. Commun.* **12**, 5186 (2021).

29. Grasby, S. E., Them II, T. R., Chen, Z., Yin, R. & Ardakani, O. H. Mercury as a proxy for volcanic emissions in the geologic record. *Earth-Science Rev.* **196**, 102880 (2019).

30. Yao, H. *et al.* Mercury Evidence of Intense Volcanism Preceded Oceanic Anoxic Event 1d. *Geophys. Res. Lett.* **48**, e2020GL091508 (2021).

31. Pyle, D. M. & Mather, T. A. The importance of volcanic emissions for the global atmospheric mercury cycle. *Atmos. Environ.* **37**, 5115–5124 (2003).

32. Lindqvist, O. & Rodhe, H. Atmospheric mercury—a review. *Tellus B* **37 B**, 136–159 (1985).

33. Cossa, D., Coquery, M., Gobeil, C. & Martin, J.-M. Mercury Fluxes at the Ocean Margins. *Glob. Reg. Mercur. Cycles Sources, Fluxes Mass Balanc.* 229–247 (1996) doi:10.1007/978-94-009-1780-4_11.

34. Amos, H. M. *et al.* Global biogeochemical implications of mercury discharges from rivers and sediment burial. *Environ. Sci. Technol.* **48**, 9514–9522 (2014).

35. Zheng, X. Y., Jenkyns, H. C., Gale, A. S., Ward, D. J. & Henderson, G. M. A climatic control on reorganization of ocean circulation during the mid-Cenomanian event and Cenomanian-Turonian oceanic anoxic event (OAE 2): Nd isotope evidence. *Geology* **44**, 151–154 (2016).

36. Friedrich, O., Erbacher, J., Wilson, P. A., Moriya, K. & Mutterlose, J. Paleoenvironmental changes across the Mid Cenomanian Event in the tropical Atlantic Ocean (Demerara Rise, ODP Leg 207) inferred from benthic foraminiferal assemblages. *Mar. Micropaleontol.* **71**, 28–40 (2009).

37. Huber, B. T., Hobbs, R. W., Bogus, K. A. & and the Expedition 369 Scientists. Proceedings of the International Ocean Discovery Program Volume 369 Australia Cretaceous Climate and Tectonics. *Proc. Int. Ocean Discov. Progr.* **369**, (2019).

38. Petrizzo, M. R. *et al.* Biotic and Paleoceanographic Changes Across the Late Cretaceous Oceanic Anoxic Event 2 in the Southern High Latitudes (IODP Sites U1513 and U1516, SE Indian Ocean). *Paleoceanogr. Paleoclimatology* **37**, e2022PA004474 (2022).

39. Petrizzo, M. R. *et al.* Exploring the paleoceanographic changes registered by planktonic foraminifera across the Cenomanian-Turonian boundary interval and Oceanic Anoxic Event 2 at southern high latitudes in the Mentelle Basin (SE Indian Ocean). *Glob. Planet. Change* **206**, 103595 (2021).

40. Bogus, K.; *et al.* Shore-based X-ray fluorescence core scanning of IODP Expedition 369 (Australia Cretaceous Climate and Tectonics) material. *Aust. Cretac. Clim. Tectonics. Proc. Int. Ocean Discov. Program, 369 Suppl. Mater.* **369**, (2019).

41. Li, Y. X., Montañez, I. P., Liu, Z. & Ma, L. Astronomical constraints on global carbon-cycle perturbation during Oceanic Anoxic Event 2 (OAE2). *Earth Planet. Sci. Lett.* **462**, 35–46 (2017).

42. Calvert, S. E. & Pedersen, T. F. Chapter Fourteen Elemental Proxies for Palaeoclimatic and Palaeoceanographic Variability in Marine Sediments: Interpretation and Application. *Developments in Marine Geology* vol. 1 567–644 (2007).

43. Jenkyns, H. C., Dickson, A. J., Ruhl, M. & van den Boorn, S. H. J. M. Basalt-seawater interaction, the Plenus Cold Event, enhanced weathering and geochemical change: deconstructing Oceanic Anoxic Event 2 (Cenomanian–Turonian, Late Cretaceous). *Sedimentology* **64**, 16–43 (2017).

44. Thibodeau, A. M. *et al.* Mercury anomalies and the timing of biotic recovery following the end-Triassic mass extinction. *Nat. Commun.* **7**, 11147 (2016).

45. Frey, F. A., Coffin, M. F., Wallace, P. J. & Weis, D. Leg 183 synthesis: Kerguelen Plateau-Broken Ridge-a large igneous province. in *Proceedings of the Ocean Drilling Program, scientific results* vol. 183 1–48 (2003).

46. Kuroda, J. *et al.* Contemporaneous massive subaerial volcanism and late cretaceous Oceanic Anoxic Event 2. *Earth Planet. Sci. Lett.* **256**, 211–223 (2007).

47. Boger, S. D. Antarctica - before and after Gondwana. *Gondwana Research* vol. 19 335–371 (2011).

48. Laugié, M. *et al.* Exploring the Impact of Cenomanian Paleogeography and Marine Gateways on Oceanic Oxygen. *Paleoceanogr. Paleoclimatology* **36**, e2020PA004202 (2021).

49. Oxburgh, R. Residence time of osmium in the oceans. *Geochemistry, Geophys. Geosystems* **2**, (2001).

50. Jones, M. M. *et al.* Abrupt episode of mid-Cretaceous ocean acidification triggered by massive volcanism. *Nat. Geosci.* **16**, 169–174 (2023).

51. Du Vivier, A. D. C., Selby, D., Condon, D. J., Takashima, R. & Nishi, H. Pacific 187 Os/ 188 Os isotope chemistry and U-Pb geochronology: Synchroneity of global Os isotope change across OAE 2. *Earth Planet. Sci. Lett.* **428**, 204–216 (2015).

52. Gale, A. S., Jenkyns, H. C., Kennedy, W. J. & Corfield, R. M. Chemostratigraphy versus biostratigraphy: data from around the Cenomanian-Turonian boundary. *J. Geol. Soc. London.* **150**, 29–32 (1993).

53. Erbacher, J., Friedrich, O., Wilson, P. A., Birch, H. & Mutterlose, J. Stable organic carbon isotope stratigraphy across Oceanic Anoxic Event 2 of Demerara Rise, western tropical Atlantic. *Geochemistry, Geophys. Geosystems* **6**, (2005).

54. Hasegawa, T. & Saito, T. Global synchroneity of a positive carbon isotope excursion at the Cenomanian/Turonian boundary: Validation by calcareous microfossil biostratigraphy of the Yezo Group, Hokkaido, Japan. *Isl. Arc* **2**, 181–191 (1993).

55. Bowman, A. R. & Bralower, T. J. Paleoceanographic significance of high-resolution carbon isotope records across the Cenomanian–Turonian boundary in the Western Interior and New Jersey coastal plain, USA. *Mar. Geol.* **217**, 305–321 (2005).

56. Matsumoto, H. *et al.* Mid-Cretaceous marine Os isotope evidence for heterogeneous cause of oceanic anoxic events. *Nat. Commun.* **13**, 1–9 (2022).

57. Li, G., Xia, G., Yi, H., Wu, C. & Wagreich, M. Climate changes as recorded in stable carbon isotopic compositions of the Late Jurassic marine sedimentary succession in the Qiangtang Basin, Northern Tibet. *J. Asian Earth Sci.* **236**, 105317 (2022).

58. Joo, Y. J., Sageman, B. B. & Hurtgen, M. T. Data-model comparison reveals key environmental changes leading to Cenomanian-Turonian Oceanic Anoxic Event 2. *Earth-Science Rev.* **203**, 103123 (2020).

59. Chen, H. *et al.* Enhanced hydrological cycle during Oceanic Anoxic Event 2 at southern high latitudes: New insights from IODP Site U1516. *Glob. Planet. Change* **209**, 103735 (2022).

60. Craig, H. Isotopic standards for carbon and oxygen and correction factors for mass-spectrometric analysis of carbon dioxide. *Geochim. Cosmochim. Acta* **12**, 133–149 (1957).

61. Sharp, Z. *Principles of stable isotope geochemistry*. (2017).

62. Tappan, H. & Loeblich, A. R. Foraminiferal Evolution, Diversification, and Extinction. *J. Paleontol.* **62**, 695–714 (1988).

63. Belford, D. J. *Upper Cretaceous foraminifera from the Toolonga calcilutite and Gingin chalk, Western Australia*. (AJ Arthur, 1960).

64. Hanzlikova, E. Microbiostratigraphy of Staré Hamry 1A borehole (Godula Formation). *Vestn. Ustred. Ust. Geol.* **44**, 175–183 (1969).

65. Holbourn, A. & Kuhnt, W. Cenomanian-Turonian palaeoceanographic change on the Kerguelen Plateau: A comparison with Northern Hemisphere records. *Cretac. Res.* **23**, 333–349 (2002).

66. Hammer, Ø., Harper, D. A. T. & Ryan, P. D. PAST: Paleontological statistics software package for education and data analysis. *Palaeontol. Electron.* **4**, 1–9 (2001).

67. Chao, A. *et al.* Rarefaction and extrapolation with Hill numbers: a framework for sampling and estimation in species diversity studies. *Ecol. Monogr.* **84**, 45–67 (2014).

68. van Peer, T. E. *et al.* Data report: revised composite depth scale and splice for IODP Site U1406. in (2017). doi:10.2204/iodp.proc.342.202.2017.

69. Jenkyns, H. C., Gale, A. S. & Corfield, R. M. Carbon- and oxygen-isotope stratigraphy of the English Chalk and Italian Scaglia and its palaeoclimatic significance. *Geol. Mag.* **131**, 1–34 (1994).
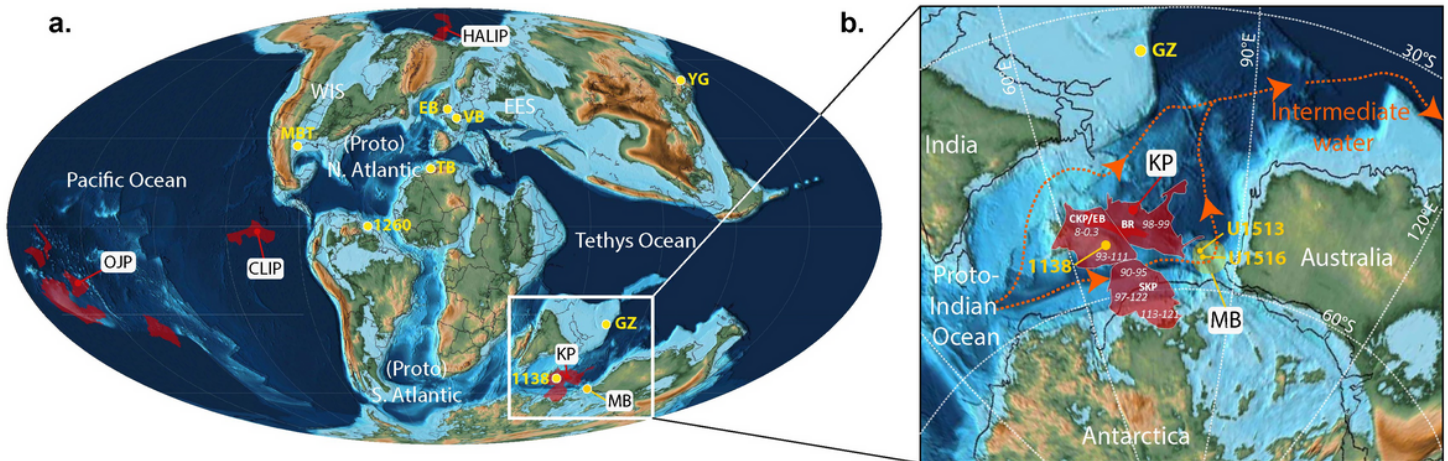
Figures

Figure 1

Paleogeographic reconstructions of the mid-Cretaceous, created on GPlates using time dependent raster files[22]. *a)* Mollweide Projection. Red shaded areas represent modelled extent of active LIPs[23]. HALIP = High Arctic Large Igneous Province; OJP = Ontong Java Plateau; KP = Kerguelen Plateau; CLIP = Caribbean Large Igneous Province; MB = Mentelle Basin; WIS = Western Interior Seaway; EES = Eurasian Epicontinental Sea; GZ = Gongzha Section, Tibet[6]; 1138 = ODP Site 1138[24]; MBT = Maverick Basin, Texas[21]; VB = Vocontian Basin, France[13]; EB = Eastbourne, UK[25]; YG =Yezo Group, Hokkaido, Japan[5]; 1260 = Site 1260 B, Demerara Rise, Atlantic Ocean[26]; TB = Tarfaya Basin, Morocco[24]. *b) The proto-Indian Ocean region focused on the Kerguelen Plateau and the Mentelle Basin. Red arrow = mean direction of intermediate water mass (500-1500m) flow during the Cenomanian[27]. Absolute ages of volcanic activity on KP and named sub-sections of the LIP[14]. NKP = North Kerguelen Plateau; BR = Broken Ridge; SKP = South Kerguelen Plateau; CKP/EB = Central Kerguelen plateau/Elan Bank.*
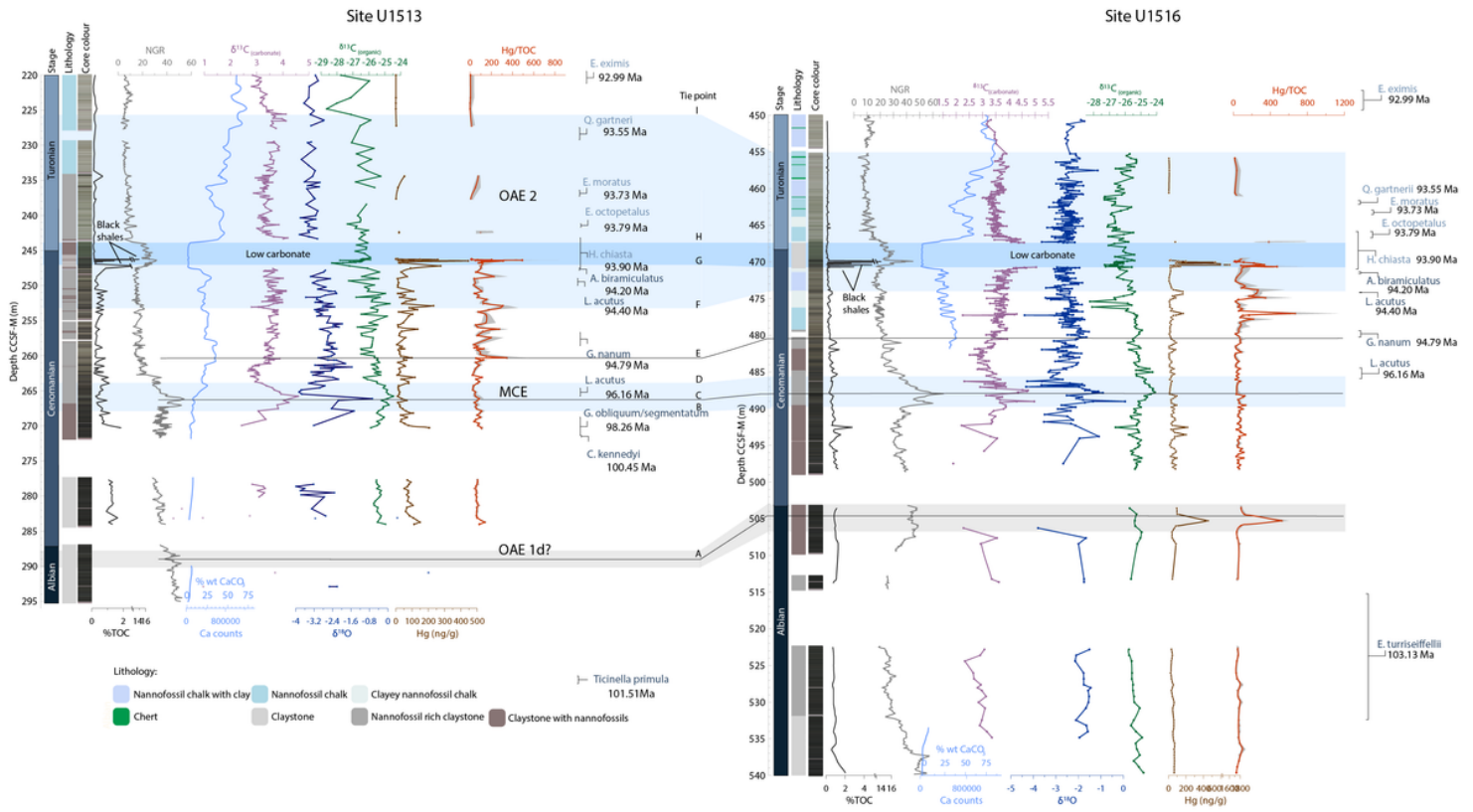
Figure 2

U1513 and U1516 Site correlation. Planktonic foraminifera and calcareous nannofossil bio-events[38,39] constrain the timing of OAE2 and the MCE. Core lithology, colour and NGR from IODP 369 Proceedings[37]. Ca counts (XRF data)[40] correlate with measured %$CaCO_3$, and the relationship between them is used to create a scale for %$CaCO_3$. CCSF (m) = core composite depth below sea floor in meters. % TOC (Total Organic Carbon), $\delta^{13}C_{(organic)}$, Hg and Hg/TOC presented in this study. $\delta^{13}C_{(carbonate)}$ is a compilation of data from this and other recent studies[38,39]. Light blue shading represents the MCE and OAE2, with darker blue shading indicating the carbonate dissolution zone in OAE2. A light grey shaded area indicates the possible location of OAE 1d (see Supplementary Materials for identification of OAEs). Grey shading in Hg/TOC data represents uncertainty – see details in methods for calculations.
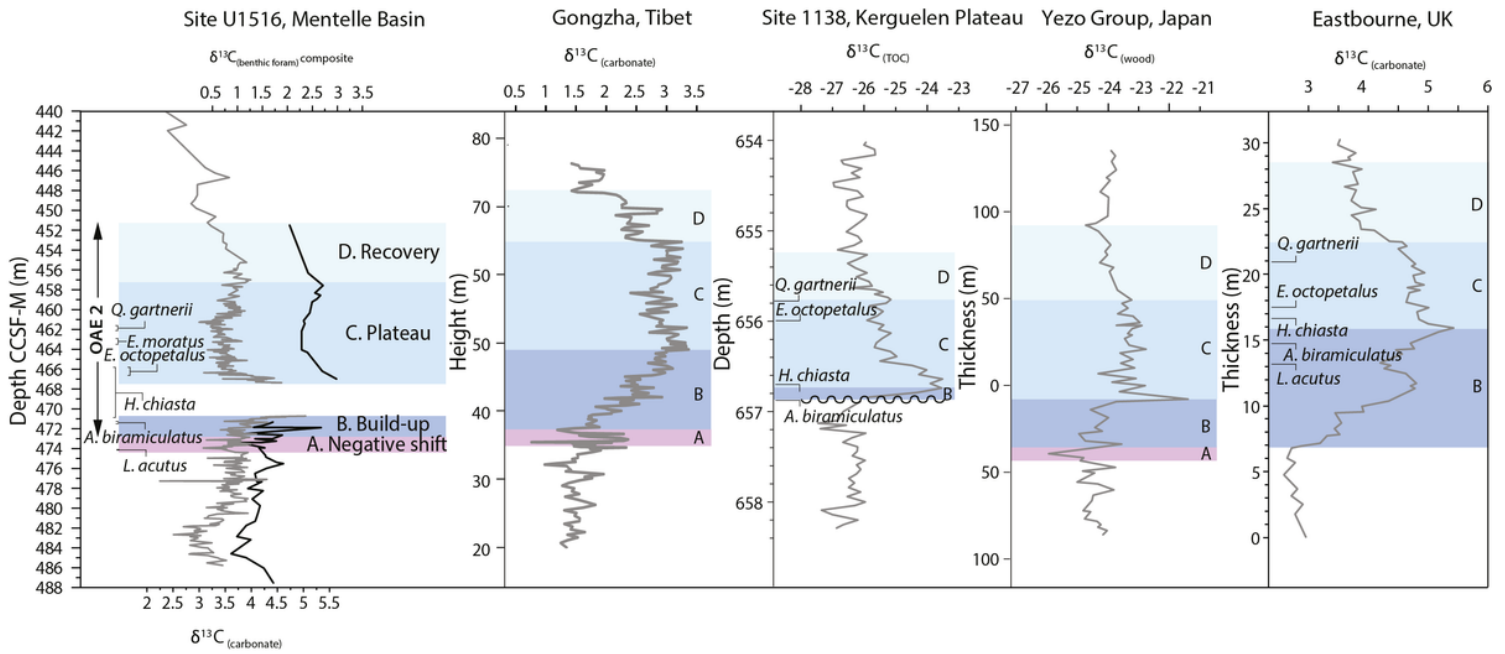
Figure 3

Refined carbon isotope stages from site U1516 in the Mentelle Basin, SW Australia, supported by biostratigraphy[38]. Bulk carbonate (grey) and benthic foraminifera δ^{13}C data (black) are shown for the Mentelle Basin – the latter showing a prolonged positive excursion compared to bulk isotope data. Colour bands indicate different carbon isotope stages of OAE2 that are used to establish correlations of the OAE2 records. Data from the Mentelle Basin (this study), Gongzha, Tingri, southern Tibet[6], ODP Site 1138 (Kerguelen Plateau)[24], Yezo Group, Japan and Eastbourne, UK[5].
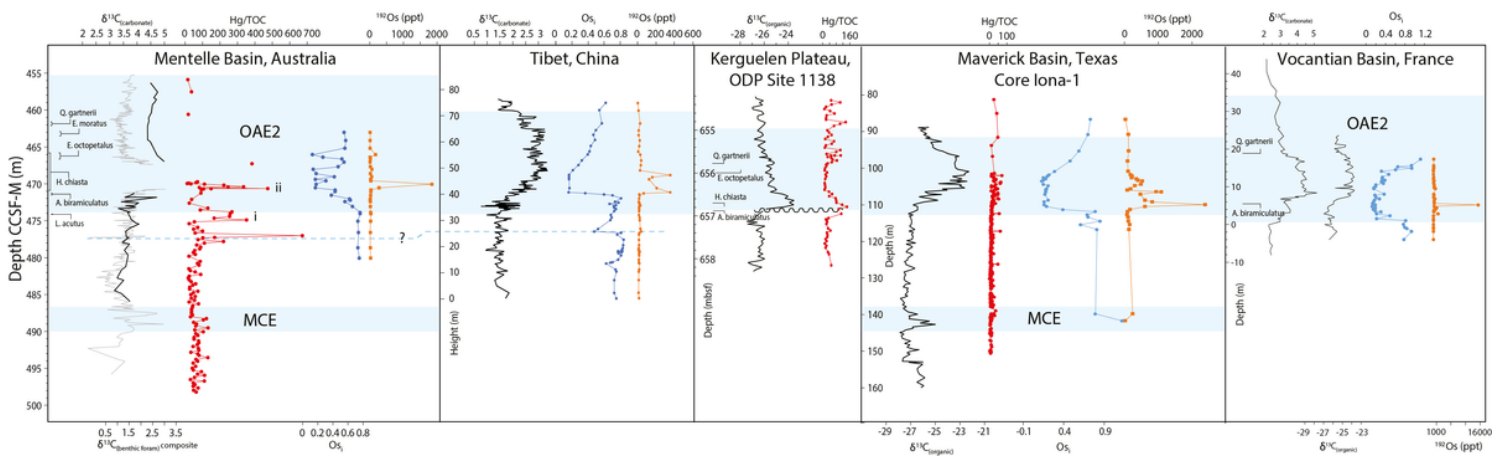

Figure 4

Hg/TOC and δ^{13}C records of OAE2 and the MCE from the Mentelle Basin (proto-Indian Ocean), Maverick Basin (WIS)[21], Tibet[6], the Kerguelen Plateau[43] and Vocontian Trough, south-east France[25]. Hg/TOC values in the Mentelle Basin are an order of magnitude higher than at Northern Hemisphere sites across OAE2, indicating a proximal source of volcanism to SW Australia. Data from the Kerguelen Plateau are incomplete due to a hiatus during OAE2 onset – precluding direct comparison with the Mentelle Basin,

and making a Kerguelen Plateau source of Hg possible, despite generally low Hg/TOC values in the upper portion of the OAE2 record from ODP Site 1138 (Kerguelen Plateau).
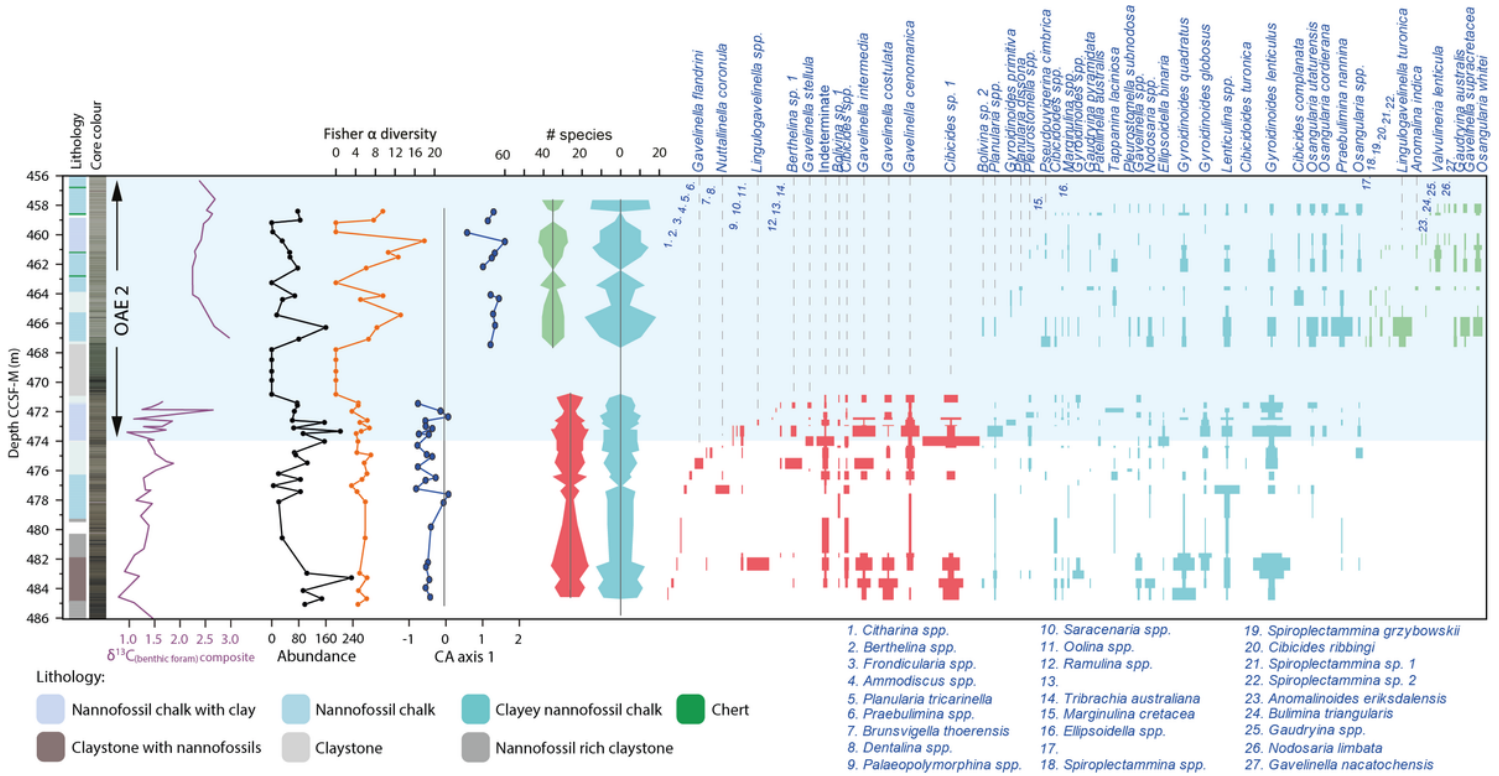

Figure 5

Site U1516 benthic foraminifera range chart, abundance, Fisher α diversity, Correspondence Analysis Axis 1, and carbon and oxygen isotope curves from benthic foraminifera and bulk carbonate. A significant shift in assemblage is seen either side of the *low carbonate* horizon. Axis 1 of the CA correlates with the proportion of infaunal / high productivity species (Supplementary data 2). Thus, high values above the dissolution horizon suggest high organic carbon flux in the later stages of OAE 2.
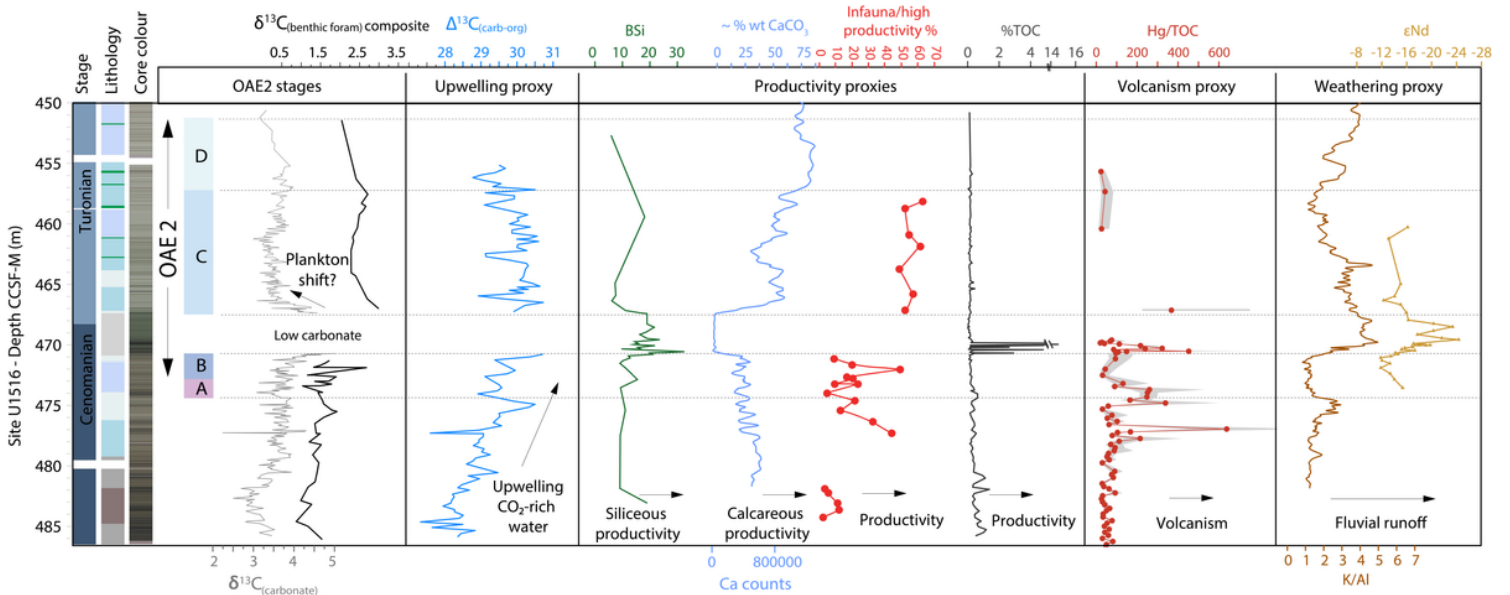
Figure 6

Summary figure showing environmental interpretations for the Mentelle Basin, Site U1516, during OAE2. Δ13C interpreted as local increased CO_2 in the surface waters – either as a result of higher atmospheric CO_2 levels or increased upwelling. $\delta^{13}C_{(carbonate)}$ and $\delta^{13}C_{(benthic\ foram)}$ composite show similar trends prior to OAE2, and during phases A and B. After the carbonate dissolution horizon, there is an offset between the two, possibly caused by a change in the dominance or abundance of different planktic groups. Hg/TOC data show sporadic enhanced volcanism prior to OAE2 onset, with the first large Hg/TOC signal occurring at OAE2 onset, corresponding with a negative shift in $\delta^{13}C$ for both bulk and composite benthic foraminiferal records. Another large spike in Hg/TOC corresponds with the start of enhanced fluvial runoff, demonstrated by K/Al and εNd data[59]. Productivity is enhanced over OAE2, and remains high during phase C, despite the apparent recovery in $\delta^{13}C_{(carbonate)}$. A particularly intense period of productivity over the carbonate dissolution horizon is suggested by high levels of biogenic silica (BSi)[50].

Supplementary Files

This is a list of supplementary files associated with this preprint. Click to download.

- Supplementarydata1geochemistry.xlsx
- Supplementarydata2benthicforaminifera.xlsx
- OceanicAnoxicEvent2triggeredbyKerguelenPlateauvolcanismSupplementarymaterials.docx